Acta Crystallographica Section B
Structural Science
ISSN 0108-7681

Electron-diffraction structure refinement of Ni_4Ti_3 precipitates in $Ni_{52}Ti_{48}$

Wim Tirry,[a]* Dominique Schryvers,[a] Kevin Jorissen[a] and Dirk Lamoen[b]

[a]Electron Microscopy for Materials Science (EMAT), University of Antwerp (UA), Groenenborgerlaan 171, B-2020 Antwerp, Belgium, and [b]TSM, University of Antwerp (UA), Groenenborgerlaan 171, B-2020 Antwerp, Belgium

Correspondence e-mail: wim.tirry@ua.ac.be

Received 22 March 2006
Accepted 8 September 2006

The atomic coordinates of the crystal structure of nanoscale Ni_4Ti_3 precipitates in Ni-rich NiTi is refined by means of a least-squares method based on intensity measures of electron-diffraction patterns. The optimization is performed in combination with density functional theory calculations and has yielded an $R\bar{3}$ symmetry with slightly different atomic positions when compared with the existing structure. The new unit cell offers a better understanding of the lattice deformation from the $B2$ matrix.

1. Introduction

Near-equiatomic NiTi alloys are often used for medical applications like stents and orthodontic wires due to their well known shape memory and superelastic behavior (Otsuka & Ren, 2005; Otsuka & Wayman, 1998). The reason why these alloys can recover their shape is because of the displacive character of the underlying martensitic transformation. The crystal transforms from a cubic ($B2$) high-temperature phase (austenite) to a monoclinic ($B19'$) low-temperature phase (martensite). This transformation can occur upon cooling or under the influence of an applied stress, in which case large strains might be obtained that can be fully recovered without plastic deformation. The properties of this transformation such as transformation temperature, number of transformation steps and whether it is superelastic or not are strongly influenced by the presence of Ni_4Ti_3 precipitates (Bataillard *et al.*, 1998; Khalil-Allafi *et al.*, 2002; Filip & Mazanec, 2001; Zel'dovich *et al.*, 1997). These precipitates have an ordered crystal structure and occur in the matrix after an appropriate heat treatment. They are enriched in Ni and have an estimated Ni:Ti = 4:3 composition ratio. The structure of these precipitates was first proposed by Tadaki *et al.* (1986) to be rhombohedral with the space group $R\bar{3}$. A morphological study by the same authors reveals a lens shape with eight orientational variants which was confirmed by Nishida *et al.* (1986) and Nishida & Wayman (1987). The replacement of some B2 Ti atoms by Ni results in a rhombohedral distortion since the Ni-atom radius is smaller than that of Ti. The atomic positions in the unit cell proposed by Tadaki are those of the cubic structure projected into the rhombohedral one, and as already indicated by Tadaki *et al.* this is probably just an approximation of the real atomic positions. Since this structure is metastable and exists only in a solid solution with the $B2$ matrix and since the size of the precipitates is in the range of a few nm up to a few microns, it is impossible to perform X-ray or neutron diffraction on a single Ni_4Ti_3 crystal in order to refine its structure *via* kinematical refinement methods. In a TEM (Transmission Electron Microscope), however, it is possible to use a fine electron probe and obtain diffraction measurements

of a single precipitate. With the use of the recently developed MSLS (multi-slice least-squares) method by Jansen & Zandbergen (2002) and Zandbergen & Jansen (1998) it is possible to refine the crystal structure from these dynamical diffraction patterns in much the same way as is conventionally done for kinematic X-ray or neutron refinements.

In previous papers we focused on the lattice distortions and concentration gradients surrounding these precipitates (Tirry & Schryvers, 2005; Yang *et al.*, 2005). In the present paper a crystal structure refinement is performed on the atomic structure of the precipitates in combination with density functional theory (DFT) calculations to compute the energy of the different structures involved and retrieve the one which is energetically most favorable. The MSLS method was already successfully applied by Schryvers & Potapov (2002) to refine the *R*-phase occurring in Ni–Ti and essentially the same experimental conditions were used in this case. Another possibility to refine or check an atomic structure is by using atomic or high-resolution TEM (HRTEM) images and comparing those to image simulations obtained with *e.g.* the multi-slice method. Ideally, such an approach should involve the use of amplitude and phase images obtained by a holographic method such as the focus-variation method developed by Coene *et al.* (1996), which allows for a quantitative comparison. In practice, however, some conclusions can also be drawn when using conventional HRTEM images, as will be shown towards the end of this paper.[1]

2. Methodology

2.1. Experimental details

Bulk $Ni_{52}Ti_{48}$ was given a solution treatment at 1223 K for 30 min followed by water quenching and aging for 4 h at 793 K to form relatively large Ni_4Ti_3 precipitates. The complete treatment was carried out in a quartz tube under vacuum conditions. TEM specimens were prepared from the bulk material by mechanical grinding and a final electropolishing step to obtain electron transparency. Electropolishing was done with a solution of 93% acetic acid with 7% sulfuric acid at a temperature of 280 K and a potential of 20 V. The specimens show a homogeneous distribution of precipitates with a mean diameter for the central disc of $\sim$ 700 nm and a thickness below 100 nm.

The experimental part of the MSLS procedure consists of making a series of electron-diffraction pattern (DP) recordings in different crystal-zone orientations and preferably for different thicknesses of the specimen. A CM30 microscope equipped with a field emission gun and 1 K CCD camera was used to make digital recordings of the DPs. The probe size of the electron beam has a diameter of around 40 nm and the microscope was operated at 300 kV. Two suitable zone orientations were chosen: $[100]_R$ and $[111]_R$, which are parallel with the $[20\bar{1}]_{B2}$ and $[111]_{B2}$ matrix orientations, respectively, with the subscript R representing indexes in reference to the rhombohedral lattice. Other zone orientations were not suitable for two reasons: first, there should be enough superstructure spots present; second, overlap between matrix and precipitate should be avoided. In Fig. 1(*a*) the two applied zone orientations and their corresponding DP's (Fig. 1*b*) are

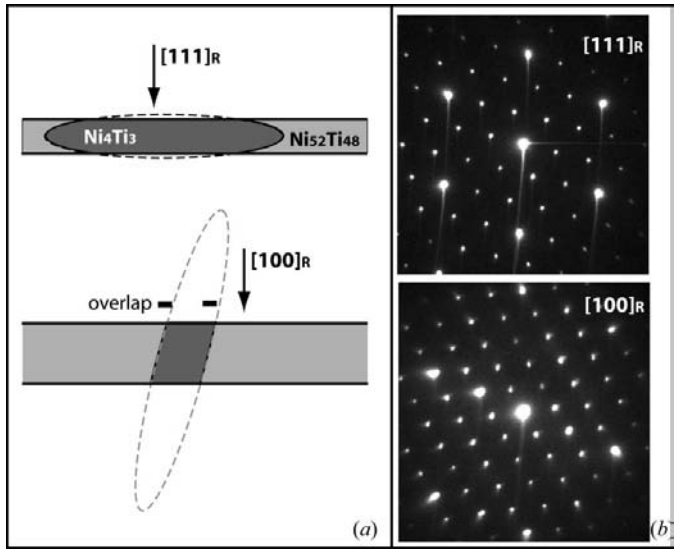

Figure 1
(*a*) Schematic representation of a sliced precipitate in a TEM specimen; the arrow indicates the direction of the incident beam for the two chosen zone orientations. (*b*) The corresponding DPs.

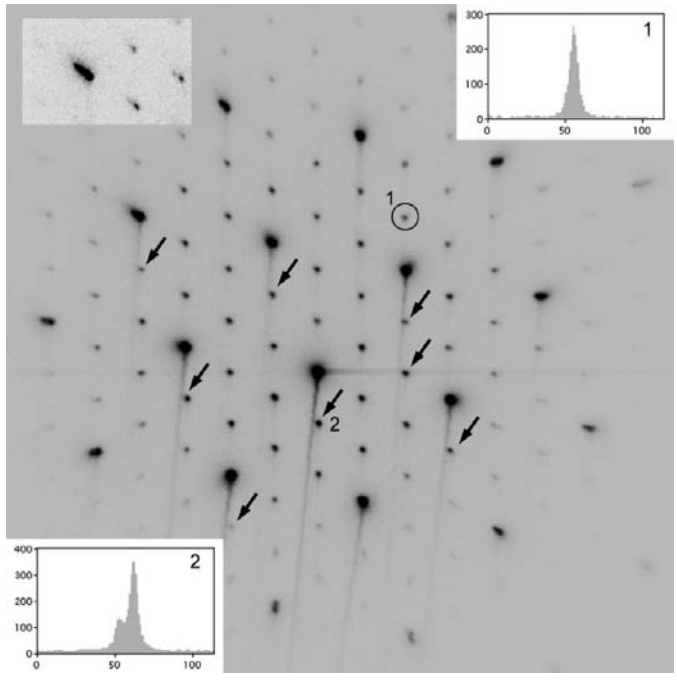

Figure 2
Example of an electron-diffraction pattern recorded on a CCD (rescaled to 256 gray values, the highlighted part in the top left shows another rescaling, especially for indicating low-intensity spots), arrows indicate excluded spots. Insets 1 and 2 show profiles through two superspots illustrating the signal-to-noise ratio and effect of a streak.

[1] Supplementary data for this paper are available from the IUCr electronic archives (Reference: LC5049). Services for accessing these data are described at the back of the journal.

Table 1
The atomic positions in the Ni_4Ti_3 rhombohedral unit cell with the space group $R\bar{3}$, as determined by Tadaki and after MSLS refinement starting from Tadaki.

	x	*y*	*z*	Occupancy
Tadaki				
Ni1	0	0	0	1
Ni2	0.5	0.5	0.5	1
Ni3	1/14	9/14	11/14	1
Ti	4/7	1/7	2/7	1
MSLS structure				
Ni1	0	0	0	1
Ni2	0.5	0.5	0.5	1
Ni3	0.0277 (15)	0.6064 (12)	0.7318 (14)	1
Ti	0.5755 (14)	0.1505 (12)	0.2793 (13)	1

graphically presented. As can be seen in Fig. 1(*a*) the precipitate–matrix interface in the $[100]_R$ zone orientation is not perfectly observed edge-on. This will result in a small overlap and care was taken that the DPs were obtained from the middle of the precipitates to avoid this overlap. For each of the two orientations 20 recordings were taken from different precipitates in the specimen. A typical diffraction pattern as recorded on a CCD and used for analysis is given in Fig. 2. Since the dynamical range of the used CCD is much larger (15 000 counts) than a normal grayscale print (256 levels), spots with low intensities can only be made visible by rescaling and thus retaining a good signal-to-noise ratio (see upper left inset in Fig. 2). Recording times were chosen in such a way that the number of electron counts of the most intense spots remains below the dynamical range of the CCD camera and the less intense spots, *e.g.* superspots and those with a higher **g** vector still have an adequate signal-to-noise ratio, as shown in inset 1 in Fig. 2. Depending on the sample thickness this resulted in recording times from 0.01 to 0.1 s, and as explained further on this will still result in the exclusion of some recorded reflections. The intensity of a reflection is measured by integrating over a surrounding circular area. The specific procedure used determines an appropriate diameter and immediately includes a background subtraction (more details are found in the works of Zandbergen & Jansen (1998). Spots of which the intensities cannot be determined correctly due to experimental errors are excluded; the rules used for exclusion are as follows:

(i) spots containing oversaturated pixels are excluded (pixel value = dynamical range CCD);

(ii) when an intense streak due to the CCD readout of very bright spots/pixels is present, the less intense spots, *e.g.* superspots, (nearly) crossed by this streak are omitted since the intensity of the streak and of the spot are of the same magnitude (as illustrated in the second inset of Fig. 2);

(iii) exclusion of spots containing dead or dying pixels which are not working correctly (determined in advance).

After exclusion, between 100 and 140 reflections remain in each recorded pattern. Moreover, only the positions belonging to the reciprocal space of the proposed structure are taken into account; even if they do not show intensity in the pattern, all the other spots present and the higher-order Laue zones are neglected. A last remark concerning the seemingly deformed spots at the edges: these distortions are due to lens aberrations and do not hinder the measurement of the total intensity of the diffracted beam as such, so they can be included if they do not fall under one of the exclusion conditions listed above.

The same CM30 microscope was used to record the atomic resolution observations on a CCD and these were again obtained in the $[111]_R$ and $[100]_R$ zone orientations. Image filtering (Wiener filter) was applied in order to reduce the noise and allow better comparison with simulations.

2.2. Computational details

The structure of crystalline (bulk) Ni_4Ti_3 was optimized within the DFT methodology using the all-electron full potential (linearized) augmented plane wave plus local orbitals (L/APW+lo) method as implemented by Blaha *et al.* (2001) in the WIEN2k code. This method uses periodic boundary conditions to model the Ni_4Ti_3 structure. For Ti the 1*s*, 2*s*, 2*p* states and for Ni the 1*s*, 2*s*, 2*p*, 3*s* states were considered as core states. The muffin–tin radii of Ni and Ti were both taken as 2.00 a.u. The RK_{max} parameter which controls the convergence of the basis set was put to 7, where R is the radius of the muffin–tin sphere and K_{max} for the magnitude of the largest reciprocal lattice vector used in the basis set. The full Brillouin zone (BZ) was sampled with 120 $\boldsymbol{k}$ points which corresponds to 12 points in the irreducible wedge of the *BZ*. The Perdew–Burke–Ernzerhof generalized gradient approximation (GGA), developed by Perdew *et al.* (1996), was used for the exchange-correlation function. These calculations assume no external stresses or other possible influences from the surrounding matrix and are performed for a temperature of 0 K.

3. Results and discussion

3.1. Refinement using MSLS and DFT

The MSLS refinement procedure requires a starting unit cell. An obvious choice for this starting structure is the structure proposed by Tadaki and presented in Table 1. For each DP the following parameters were refined before the actual refinement of the unit cell started: intensity scale factor, specimen thickness and centre of the Laue circle. The MSLS procedure also refines the absorption factor as well as Debye–Waller factors; the latter is an iterative procedure with the thickness. Patterns for which these parameters could not be refined to an R factor below 0.25 were excluded from the set since this means that the DP might be originating from a matrix–precipitate overlap region or suffering from other experimental errors. The final set consisted of six patterns, three from each of the two zones, with a total of 651 reflections, and was used to optimize the atomic positions. These patterns also contain enough variation in thickness and the centre of the Laue circle which is important for the refinement procedure. Using the atomic coordinates as determined by Tadaki *et al.* and more accurate lattice parameters a =

Table 2
The structure optimized with DFT starting from Tadaki and MSLS refinement starting from the structure obtained by DFT.

	x	*y*	*z*	Occupancy
DFT structure				
Ni1	0	0	0	1
Ni2	0.5	0.5	0.5	1
Ni3	0.061 (7)	0.585 (7)	0.744 (7)	1
Ti	0.505 (7)	0.109 (7)	0.242 (7)	1
DFT + MSLS structure				
Ni1	0	0	0	1
Ni2	0.5	0.5	0.5	1
Ni3	0.0605 (17)	0.5931 (11)	0.7574 (20)	1
Ti	0.4989 (10)	0.1125 (16)	0.2513(16)	1

0.6695 nm and $\alpha = 113.838^\circ$ extrapolated from values obtained with neutron diffraction by Khalil-Allafi *et al.* (2004) results in an *R* factor of 0.125 for this data set. During the refinement of this starting structure the $R\bar{3}$ symmetry was maintained, which implies that only the positions of the Ni3 and the Ti atomic sites are optimized resulting in a new structure as given in Table 1, and further referred to as the 'MSLS structure'. This new structure has an *R* factor of 0.092 which is indeed better than the original Tadaki structure. Although the MSLS method refines the structure by minimizing the *R* factor, the final structure may still depend on the initial one because of the local minima of *R*. Therefore, the DFT optimized structure was considered as an alternative starting point.

The equilibrium (bulk) structure for Ni_4Ti_3 was found by first optimizing the lattice parameters of the Tadaki unit cell, for fixed atom positions. The total energy was minimized as a function of the lattice parameters by performing a series of self-consistent total energy calculations. The energy was converged up to 0.010 meV per atom. Subsequently, the internal atom positions were relaxed within the $R\bar{3}$ space-group symmetry for lattice parameter values with energies close to or corresponding to the lowest energy. The equilibrium atomic positions followed from the minimization of the forces on the atoms by using the PORT method (a reverse-communication trust-region Quasi–Newton method), as implemented in the WIEN2k code. An additional optimization of the lattice parameters showed that the obtained structure indeed corresponds to a minimum in energy, *i.e.* no further iterative optimization of the lattice parameters and atom positions was necessary. The lattice parameters obtained for the rhombohedral cell resulting from this optimization are $a = 0.6697 \pm 0.0011$ nm and $\alpha = 113.84 \pm 0.05^\circ$. The corresponding relaxed atom positions are given in Table 2 and labeled 'DFT structure'. Increasing the number of $\boldsymbol{k}$ points to 250 in the full BZ (38 points in the irreducible part) and extending the basis set by taking $RK_{max} = 8$ did not alter the values obtained for the lattice parameters and atomic positions and showed that the relative energies are converged within 0.002 eV per atom. Computing the *R* factor for this structure in reference to the same data set, after refinement of thickness, the centre of the Laue circle and the scale factor results in $R = 0.087$, which is lower than the two structures discussed above. Further refinement of this structure with MSLS, again maintaining the $R\bar{3}$ symmetry, resulted in a final structure as given in Table 2 and referred to as the 'DFT + MSLS structure' with $R = 0.082$.

When looking in detail at the final refinement parameters given in Table 3 it can be seen that the $[111]_R$ experimental patterns show a better *R* factor than the $[100]_R$ patterns. Still, the *R* factors of the $[100]_R$ zone seem to give the largest input information for the refinement since their *R* factor decreases the most. The reason why these are not refined to an even better *R* factor could be due to a remaining small contribution of the matrix in some of the $[100]_R$ patterns, as already mentioned (see also Fig. 1*b*). Fortunately, since this contribution is different for each pattern it can be considered as random noise added to the data and appears not to be too large to inhibit the correct interpretation of the refinement. The largest reduction in the *R* factor for the $[111]_R$ zone occurs for the thickest area as here the effect on the superspots is most clear, although it should be mentioned that this thickness is at the verge of the validity of the MSLS method (Jansen *et al.*, 1998; Jansen & Zandbergen, 2002).

Other attempts to refine the structure to an *R* factor smaller than 0.08 were made by leaving out the centre of symmetry and using the *R*3 space group. However, within the precision of our calculations, neither the MSLS nor the DFT approach results in a new structure, so the system essentially conserves inversion symmetry.

Up to now possible deviations from the 4/3 composition were neglected: Nishida *et al.* (1986) measured the composition of the precipitate with EDX (energy-dispersive X-rays) as $Ni_{14}Ti_{11}$. This 14/11 ratio does not allow filling each position in the proposed unit cell with an occupancy of 1, since in the latter case the ratio becomes 4/3. This can be solved by assuming that the Ni positions are not always completely filled, *i.e.* vacancies exist, which can be incorporated by refining the occupancies of the Ni sites. In the MSLS refinement procedure the Ni and also the Ti site occupancies were refined for both the MSLS structure and the DFT + MSLS structure: this, however, again did not result in a lower *R* factor and so the composition is kept at 4/3. Recent EELS (electron-energy loss spectroscopy) measurements performed by Yang & Schryvers (2006) also confirm the 4/3 ratio within a 2% error margin.

A résumé of the *R* factors and computed energies for the four structures is given in Table 4 the energies have values relative to the DFT structure. By comparing the *R* factors it can be seen that the optimization from the Tadaki structure towards the DFT + MSLS structure results in a decrease of the *R* factor by 0.043. Nevertheless, it should be realised that all three newly found structures are manifesting a good improvement in the *R* factor, so none of them should be rejected using this information only. Comparing the energies shows that the MSLS structure is higher in energy than the Tadaki structure by +0.045eV per atom and higher than the DFT and DFT + MSLS structures. This, in combination with the slightly higher *R* factor, allows us to reject the MSLS structure. It is not possible to use a similar argument to discriminate between the DFT and DFT + MSLS structures,

Table 3
Final refined data set for structure (III) consisting of three $[100]_R$ and $[111]_R$ zones.

For each pattern the refined scale factor, thickness and centre of Laue is given. The *R* factor of each pattern is compared with the corresponding one of the original Tadaki structure.

Zone	Scale	Thickness (nm)	Centre of Laue			DFT + MSLS *R* factor	Tadaki *R* factor
			h	*k*	*l*		
[100]	0.77	7.0 (7)	0	−2.1 (5)	2.6 (5)	0.13	0.188
[100]	0.86 (3)	10.7 (6)	0	−0.88 (9)	0.73 (6)	0.071	0.144
[100]	0.89	33.6 (4)	0	−0.40 (5)	0.42 (4)	0.099	0.162
[111]	1.50 (5)	20.8 (3)	0.006 (13)	0.15 (3)	−0.16 (3)	0.071	0.072
[111]	0.93 (4)	20.1 (3)	0.081 (18)	−0.12 (2)	0.04 (3)	0.045	0.057
[111]	1.34 (5)	44.7 (6)	−0.23 (3)	0.33 (5)	−0.09 (6)	0.079	0.12

Table 4
The calculated *R* factor for the four structures after refinement of specimen thickness, centre of Laue and scale factor.

ΔE is the relative energy in reference to the DFT structure.

	R factor	ΔE (eV per atom)
Tadaki	0.125	0.090 ± 0.002
MSLS	0.092	0.135 ± 0.002
DFT	0.087	0
DFT + MSLS	0.082	0.028 ± 0.002

since they are too close to each other both in *R* factor and energy. However, as noted before, it should be emphasized that the DFT calculations are performed at $T = 0$ K and on a stress-free structure. The fact that GGA yields the experimentally observed lattice parameters, whereas in general this approach is known to have the tendency to overestimate lattice parameters (Staroverov *et al.*, 2004), could be due to the fact that the calculations are carried out on bulk Ni_4Ti_3 and the measurements itself are performed on precipitates embedded in a strained matrix. These precipitates are thus exposed to a tensile stress due to the precipitate matrix mismatch. From the Eshelby solution for elliptical inclusions, described in the work of Mura (1982), it is known that there is indeed a uniform strain field in the inclusion which implies that the measured parameters will be somewhat larger than those calculated in a stress-free condition. A general overestimation of the lattice parameters in the GGA approach might thus accidentally compensate for this difference between measuring in tensile-strained precipitates and calculating under stress-free conditions. It should be noticed that a similar DFT optimization of the structure with the exchange-correlation potential taken in the Local Density Approximation (Perdew & Wang, 1992) yields $a = 0.658$ nm and $\alpha = 113.95°$. This value for *a* is too low compared with the experiment, which is a well known artifact of the LDA approximation. However, it must be stressed that the relaxed atom positions are essentially the same as those optimized with the GGA exchange and correlation potential. As MSLS accounts for the effect of external stress and temperature which is incorporated in the experimental data and has a somewhat more favourable *R* factor, the DFT + MSLS structure is considered to be the most realistic one for Ni_4Ti_3 precipitates embedded in a *B*2 matrix.

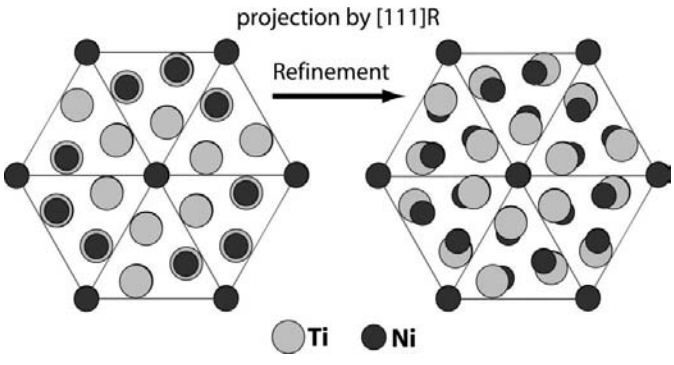

Figure 3
Projected structure of Ni_4Ti_3 in the $[111]_R$ direction before (Tadaki) and after refinement (structure DFT + MSLS).

3.2. Evaluation of the refined structure

Comparing the Tadaki structure with the newly optimized structure it is seen that the absolute positions and distances between neighboring atoms differ significantly. When the DFT + MSLS structure is projected along the $[111]_R$ direction, as shown in Fig. 3, it is seen that the columns consisting of the sequence Ni–Ti–Ni–Ti–... are distorted; the atomic centers no longer perfectly overlap as is the case for the Tadaki structure. The position of Ti is moved over 0.035 nm, which is 5.2% of the lattice constant, while Ni3 is moved over a distance of 0.027 nm equal to 4.0% of the lattice constant. As a result the Ti atoms are now more widely spaced, since the distance between the two nearest-neighbor Ti atoms increases from 0.298 to 0.308 nm. In the case of the Ni3 atoms this distance decreases from 0.298 to 0.269 nm, while for the Ni2 atoms the nearest-neighbor distance remains 0.254 nm. The reason why the Ni and Ti atom centers are no longer on a straight line is related to the shrinking of the unit cell. In the $[111]_R$ direction the rhombohedral structure contracts 2.9% in reference to the matrix, which is normally explained by the substitution of a large Ti atom by a smaller Ni atom. Owing to this substitution some atom columns in the $[111]_R$ direction contain only Ni. For these columns it is evident that the interatomic distance is shorter, but the other columns have the same composition and sequence as in the B2 structure and it would not be energetically favorable to contract these in the same direction. By moving away in different directions from the central $[111]_R$ axis the component of the interatomic distance in the $[111]_R$ direction can become smaller. This explains the contraction of almost 3% in this direction in a more complete way than only giving credit to the smaller size of the Ni atom in one of the columns.

Finally, atomic resolution images are compared to multislice simulations, obtained with the *MacTempas* (Kilaas, 2004) software package, for the Tadaki and the DFT + MSLS

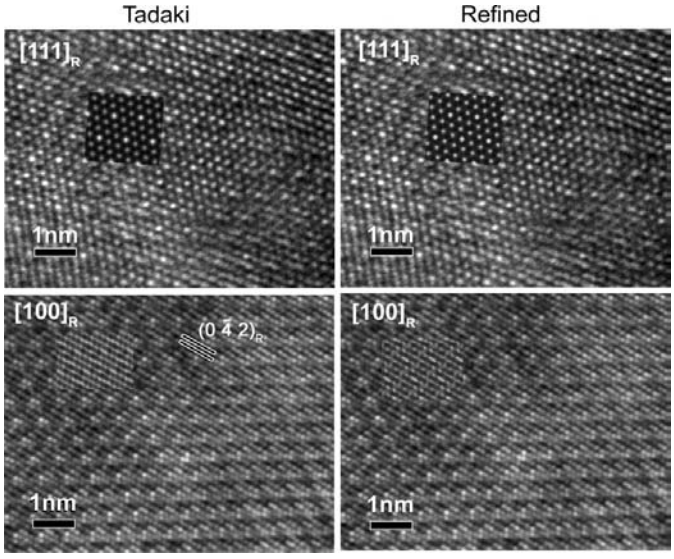

Figure 4
Atomic resolution images of the $[111]_R$ and $[100]_R$ zone, the left and right column showing simulation insets of, respectively, the Tadaki and refined structure.

structure. The $[111]_R$ and $[100]_R$ zones are particularly considered here, although similar results hold for other zone orientations. Fig. 4 shows experimental observations with simulations presented as an inset. In the case of the $[111]_R$ zone, both simulations reveal a good comparison with the experimental image and this holds for different thickness and defocus values. In the case of the $[100]_R$ zone, the Tadaki structure always (*i.e.* for all thickness and defocus values used) shows quasi-continues lines for the $(0\bar{4}2)$ planes, whereas for the refined structure these planes reveal a resolved image of elongated dashes for some combinations of thickness and defocus, corresponding to the presented experimental image. It can thus be concluded that the conventional high-resolution images confirm the newly refined atomic coordinates.

As the present refinement deals with the internal atomic structure of the precipitates, it will most probably not have a significant direct effect on understanding the role of the Ni_4Ti_3 precipitates in the shape memory and superelastic behavior of this alloy. However, in ongoing research we are now focusing on the atomic structure of the interface between the precipitate and the matrix, which can be expected to be of greater relevance to the martensitic transformation of the matrix. In order to develop a proper atomic model for this interface, knowledge of the exact atomic structure of both phases involved is of course indispensable.

4. Conclusions

The atomic positions of the Ni_4Ti_3 precipitates in Ni-rich NiTi are refined using the multi-slice least-squares method based on measured intensities of electron-diffraction patterns. The best refinement in terms of the resulting *R* factor is obtained when starting from the equilibrium bulk structure calculated by density functional theory, starting from the original Tadaki unit cell. The atomic positions in the final refined structure are consistent with the overall compression of the lattice in the precipitates. No improvement was found when lowering the symmetry or changing the 4:3 composition.

K. Jorissen gratefully acknowledges financial support from the F. W. O. Vlaanderen. Part of this work was performed with the support of a European project 'Multi-scale modelling and characterization for phase transformations in advanced materials' a Marie Curie Research Training Network (MRTN-CT-2004–505226).

References

Bataillard, L., Bidaux, J.-E. & Gotthardt, R. (1998). *Philos. Mag. A*, **78**, 327–344.
Blaha, P., Schwarz, K., Madsen, G. K. H., Kvasnicka, D. & Luitz, J. (2001). *Wien2k*. Technische Universität Wien, Austria.
Coene, W. M. J., Thust, A., Op de Beeck, M. & Van Dyck, D. (1996). *Ultramicroscopy*, **64**, 109–135.
Filip, P. & Mazanec K. (2001). *Scr. Mater.* **45**, 701–707.
Jansen, J., Tang, D., Zandbergen, H. W. & Schenk, H. (1998). *Acta Cryst.* A**54**, 91–101.
Jansen, J. & Zandbergen, H. W. (2002). *Ultramicroscopy*, **90**, 291–300.
Khalil-Allafi, J., Dlouhy, A. & Eggeler, G. (2002). *Acta Mater.* **50**, 4255–4274.
Khalil-Allafi, J., Schmahl, W. W., Wagner, M., Sitepu, H., Toebbens, D. M. & Eggeler, G. (2004). *Mater. Sci. Eng. A*, **378**, 161–164.
Kilaas, R. (2004). *MacTempas*, Version 2.1.1.
Mura, T. (1982). *Micromechanics of Defects in Solids*. Boston: Nijhoff.
Nishida, M. & Wayman, C. M. (1987). *Mater. Sci. Eng.* **93**, 191–203.
Nishida, M., Wayman, C. M. & Honma, T. (1986). *Metall. Trans. A*, **17**, 1505–1515.
Otsuka, K. & Ren, X. (2005). *Progress Mater. Sci.* **50**, 511–678.
Otsuka, K. & Wayman, C. M. (1998). *Shape Memory Materials*. Cambridge University Press.
Perdew, J. P., Burke, K. & Ernzerhof, M. (1996). *Phys. Rev. Lett.* **77**, 3865–3868.
Perdew, J. P. & Wang, Y. (1992). *Phys. Rev. B*, **45**, 13244–13249.
Schryvers, D. & Potapov, P. L. (2002). *Mater. Trans.* **43**, 774–779.
Staroverov, V. N., Scuseria, G. E., Tao, J. & Perdew, J. P. (2004). *Phys. Rev. B*, **69**, 075102.
Tadaki, T., Nakata, Y., Shimizu, K. & Otsuka, K. (1986). *JIM*, **27**, 731–740.
Tirry, W. & Schryvers, D. (2005). *Acta Mater.* **53**, 1041–1049.
Yang, Z. & Schryvers D. (2006). Proc. of ESOMAT 2006.
Yang, Z., Tirry, W. & Schryvers, D. (2005). *Scr. Mater.* **52**, 1129–1134.
Zandbergen, H. W. & Jansen, J. (1998). *J Microsc. Oxford*, **190**, 222–237.
Zel'dovich, V., Sobyanina, G. & Novoselova, T. V. (1997). *J. Phys. IV Fr.* **7**, 299–304.